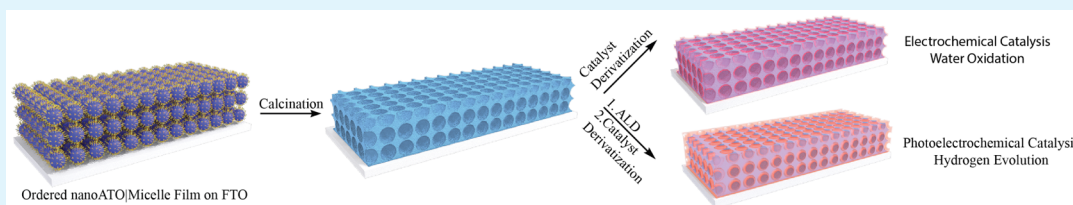


High Surface Area Antimony-Doped Tin Oxide Electrodes Tempered by Graft Copolymerization. Applications in Electrochemical and Photoelectrochemical Catalysis

Hanlin Luo,[†] Zhen Fang,[†] Na Song,[†] Timothy Garvey,[‡] Rene Lopez,[‡] and Thomas J. Meyer*,[†]

[†]Department of Chemistry and [‡]Department of Physics and Astronomy, University of North Carolina at Chapel Hill, Chapel Hill, North Carolina 27599-3290, United States

Supporting Information



ABSTRACT: Mesoporous ATO nanocrystalline electrodes of micrometer thicknesses have been prepared from ATO nanocrystals and the grafted copolymer templating agents poly vinyl chloride-g-poly(oxyethylene methacrylate). As-obtained electrodes have high interfacial surface areas, large pore volumes, and rapid intraoxide electron transfer. The resulting high surface area materials are useful substrates for electrochemically catalyzed water oxidation. With thin added shells of TiO₂ deposited by atomic layer deposition (ALD) and a surface-bound Ru(II) polypyridyl chromophore, they become photoanodes for hydrogen generation in the presence of a reductive scavenger.

KEYWORDS: antimony doped tin oxide, graft copolymer template, water oxidation, atomic layer deposition, photoanode

INTRODUCTION

Transparent conducting oxides (TCOs) have been successfully utilized in a wide range of optoelectronic and photoelectrochemical applications.^{1,2} 3-D mesoporous nanostructured TCO (*nano*TCO) films, typically with pore diameters between 2 and 50 nm, have greatly increased surface areas and undergo faster drift electron transport than the diffusive transport found in traditional metal oxide semiconductors like TiO₂.^{3,4} These properties impart *nano*TCO electrode films with properties that could be of value in a variety of applications – dye sensitized solar cells (DSSCs), electrochemical catalysis, and biochemical and optical sensors.^{5–9} The most popular *nano*TCO to date has been tin-doped indium oxide (ITO), but developing alternatives is important given the high cost and rarity of indium metal.¹⁰ Antimony-doped tin oxide (ATO) has high transparency with a large band gap (>3.6 eV), an inexpensive source, and good electrical conductivity, making it an appealing target for alternative to *nano*TCO strategy.¹¹

The most common synthetic route to 3-D mesoporous ATO is based on an inorganic metal precursor soft templated by organic surfactant molecules or amphiphilic copolymers by evaporation induced self-assembly (EISA).^{12–14} In order to explore large-pore mesoporous materials, amphiphilic copolymers are often chosen to take advantage of the microphase separation between their thermodynamically incompatible subunits.^{15,16} In spite of the elegance of this approach, it suffers from significant limitations. Complications arise from the rapid hydrolysis and condensation of mixed Sn and Sb

precursors, making it difficult to control the interaction with organic copolymers.⁹ In addition, as-obtained mesoporous structures are usually amorphous and require postannealing at elevated temperature to increase crystallinity. Annealing can also lead to strain-induced collapse of the original mesopores.¹² These limitations decrease the number of suitable choices as structure directing polymers for mesoporous ATO films to poly(ethylene-co-butylene)-*b*-poly(ethylene oxide) KLE copolymer, polyisobutylene-*b*-poly(ethylene oxide) copolymer, poly(*N,N*-dimethylacrylamide)-*b*-block-polystyrene (PDMA-PS), and pluronic block copolymer F127.^{9,17,18}

To overcome this limitation, mesoporous materials based on presynthesized ATO nanocrystals have been proposed. Müller et al. have obtained mesoporous ATO films with presynthesized, small ATO nanoparticles through traditional sol-gel techniques and the templating agent F127 copolymer.^{19,20} However, pluronic copolymers normally decompose at relatively low temperatures relative to the high temperatures required to maintain the high crystallinity of the metal oxides. Moreover, small PPO subunits in pluronic copolymers are unfavorable for large pore sizes.^{12,21} Thus, there is a need to explore nonpluronic copolymers with higher glass transition temperatures and better thermostability in the synthesis of ATO electrodes with larger mesopores.

Received: July 14, 2015

Accepted: October 21, 2015

Published: October 21, 2015

Scheme 1. Schematic Illustration of Mesoporous ATO Film Fabrication and Its Application in Electrochemical Catalysis for Water Oxidation and Photoelectrochemical Catalysis for Hydrogen Evolution

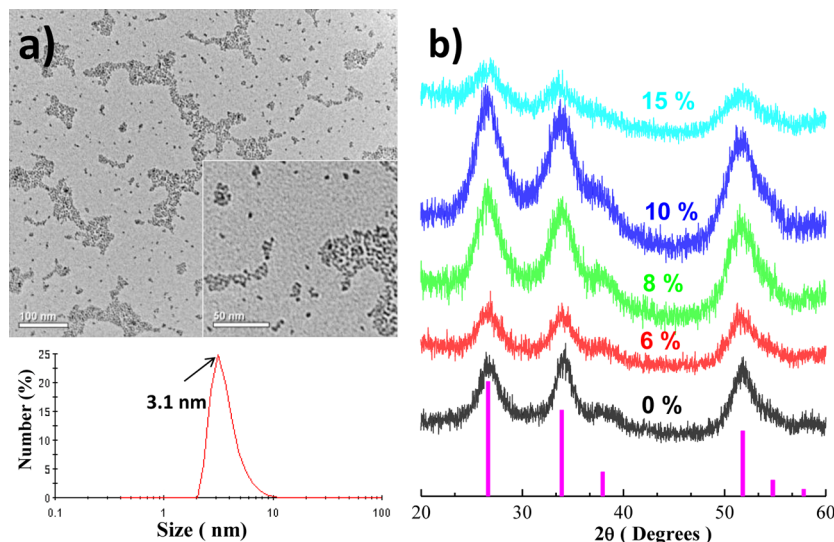
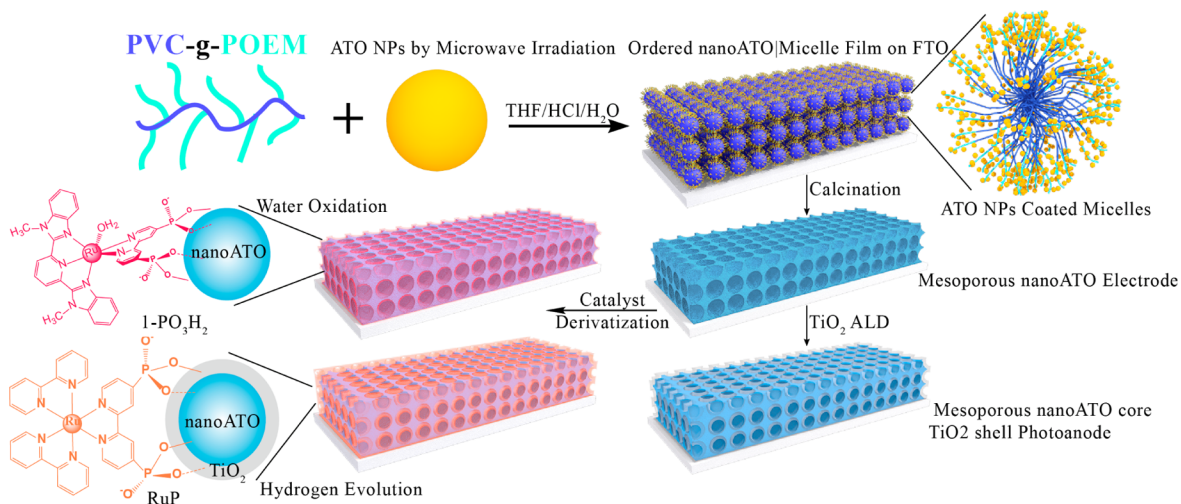


Figure 1. (a) Illustrating morphology and size of 8% ATO nanoparticles. Upper: TEM of ATO nanoparticles at low and high magnification (inset) after dispersion in THF on a copper grid. Below: size distribution of the ATO nanoparticles in THF from a DLS measurement. (b): X-ray diffraction diagrams with varying antimony content. The bars below the XRD patterns indicate the position and diffraction lines of SnO_2 cassiterite ($P4_2/mnm$, PDF No. 41-1445). All nanoparticles were prepared at 150 °C by microwave irradiation for 20 min.

In the present study, mesoporous ATO 3-D electrodes have been fabricated based on ATO nanocrystals and the structure-directing copolymer, poly(vinyl chloride)-g-poly(oxyethylene methacrylate) (PVC-g-POEM) (Scheme 1). The graft copolymer was prepared by a facile one pot atom transfer radical polymerization (ATRP) reaction. The use of this graft copolymer has already been described in the preparation of TiO_2 electrodes with large mesopores for applications in solid state dye sensitized solar cells (DSSCs).^{22,23} Compared to blocked copolymer templating agents such as polybutadiene-block-poly(ethylene oxide) (PB-PEO) and PDMA-*b*-PS,^{24,18} graft copolymers are advantageous due to their low cost and ease of synthesis. When exposed to a selective solution mixture, PVC-g-POEM copolymer forms organized micellar structures with a hydrophobic PVC core and hydrophilic POEM corona. In our procedure, freshly prepared ATO nanoparticles (yellowish) are tethered with POEM corona and further assembled into well-organized nanoATO|micelle superstruc-

tures. Mesoporous ATO nanocrystalline films are achieved after polymer removal by calcination, accompanied by a color change to blue. Mesoporous ATO electrodes with satisfactory transparency, surface area, and resistivity were optimized by varying antimony doping level from 6–15%.

The micrometer-thick, mesoporous nanoATO films obtained from this procedure undergo rapid internal electron transfer and are useful substrates as alternatives to *nanoITO* electrodes. Their efficacy as electrodes was demonstrated by an investigation of water oxidation electrocatalysis at nanoATO electrodes derivatized by the ruthenium water oxidation catalyst, $[\text{Ru}^{II}(\text{Mebimipy})(4,4'-(\text{PO}_3\text{H}_2)_2\text{bpy}) (\text{OH}_2)]^{2+}$ (1- PO_3H_2 : Mebimipy is 2,6-bis(1-methylbenzimidazol-2-yl)-pyridine, Scheme 1.). They also are used to prepare a core/shell photoanode consisting of a mesoporous ATO core with a thin semiconductor oxide shell of TiO_2 . The *nanoITO* core/shell configuration has been successfully applied in DSSCs and dye sensitized photoelectrosynthesis cells (DSPEC) for water

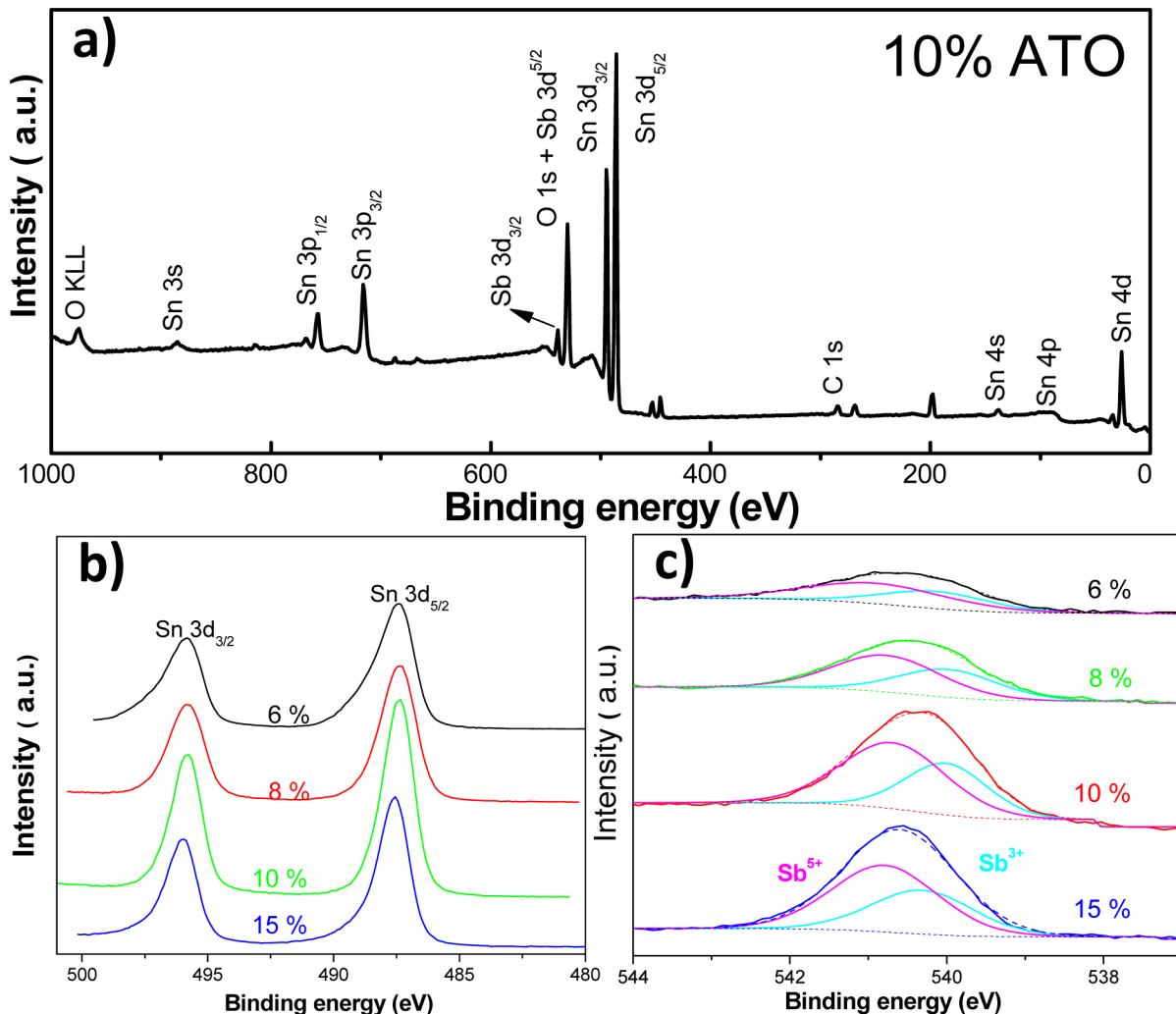


Figure 2. XPS results of as-synthesized ATO nanoparticles with varying Sb doping ratios from 6–15% at 150 °C for 20 min under microwave irradiation. (a): an overview XPS spectrum of 10% ATO nanoparticles. High resolution scans of (b) Sn 3d doublet and (c) Sb 3d_{3/2} of ATO nanoparticles. The solid lines represent experimental results, the dotted lines indicate background, and the dashed lines correspond to Gaussian peak fits. The Sb⁵⁺ and Sb³⁺ peaks are shown in magenta and cyan, respectively.

splitting. In these applications advantage is taken of the electron transport characteristics at the core/shell interface.^{4,25–27}

Here, we describe the preparation of mesoporous ATO films coated with a thin shell of TiO₂ by atomic layer deposition (ALD) with the resulting core/shell structure derivatized by a ruthenium chromophore, [Ru^{II}(bpy)₂(4,4'-(PO₃H₂)₂bpy)]²⁺(RuP²⁺, Scheme 1). The resulting hybrid core/shell molecular assembly functions as a photoanode in a DSPEC for generating H₂ in the presence of the reductive scavenger ethylenediaminetetraacetic tetra-anion (EDTA⁴⁻) under visible light illumination. The efficiency of H₂ production was comparable to efficiencies obtained with a 5 μm nanoTiO₂ film under the same conditions due to rapid scavenging of -RuP³⁺ as it is formed on the surface following excitation and injection.

RESULTS AND DISCUSSION

ATO nanoparticle synthesis utilized a microwave assisted, nonaqueous sol–gel method that is advantageous for slow sol–gel hydrolysis and condensation of metal precursors in the absence of water.^{28,29} In this procedure, benzyl alcohol was chosen as solvent to serve both as a labile nucleophile and as a

suitable solvent for microwave reaction due to its high boiling point and high dielectric loss factor.^{30–32} In a similar route as Niederberger et al.,³³ ATO nanocrystals with fine-tuning of the Sb doping ratio were successfully obtained by microwave irradiation (Supporting Information, SI). This technique substantially reduced reaction times from several days or hours^{20,34} to 20 min with Sb(acetate)₃ as the precursor. As shown in Figure 1a, the small 8% doped ATO nanoparticles obtained were only loosely agglomerated and characterized by a narrow size distribution. The average size of the particles was ~3.2 nm from TEM measurements consistent with the DLS size distribution peaking at 3.1 nm. A further increase in temperature (from 150 to 190 °C) and reaction time (from 20 to 60 min) had little effect on enlarging particle size probably due to the high concentration of initial nucleation centers under the rapid thermal/kinetic conditions in the microwave reactor.

Similarly, small monodispersed nanoparticles were synthesized with Sb ranging from 0% to 15%. The corresponding X-ray diffraction (XRD) patterns (Figure 1b) can be assigned to the cassiterite structure of SnO₂ (PDF No. 41-1445). This result shows that SnO₂ cassiterite can accommodate up to 15%

Sb dopant without conversion to another crystalline phase. The broadening of XRD peaks is consistent with the small size of the ATO nanoparticles.

The presence of only Sn, Sb, and O with a small amount of residual Cl in ATO nanocrystals with 6%, 8%, 10% and 15% antimony doping was determined by XPS analysis. A spectrum for a 10% ATO sample is shown in Figure 2. The binding energies at 487.4 and 496.0 eV arise from Sn 3d_{5/2} and Sn 3d_{3/2}, respectively. Since the binding energies for O 1s overlap with Sb 3d_{5/2} at ~531 eV, the Sb 3d_{3/2} energies were employed to quantify the antimony content by Gaussian deconvolution into components centered at 540.7 eV for Sb⁵⁺ and 540.0 eV for Sb³⁺, respectively. The total antimony doping content from XPS analysis is in good agreement with results obtained by EDS (Table 1). This is important in demonstrating that the

Table 1. Properties of ATO Nanoparticles with Different Sb Doping Levels

Sb % in the precursor solution (mol %)	Sb % in ATO nanoparticles (mol %)		molar fraction of Sb ⁵⁺ and Sb ³⁺ atoms % ^a		mesoporous ATO films templated by PVC-g-POEM resistivity Ω·cm ^b	
	by XPS	by EDS	Sb ⁵⁺	Sb ³⁺	G1	G2
6	5.6	6.2	61.3	38.7	34	54
8	7.8	8.2	58.6	41.4	44	58
10	9.9	10.0	61.7	38.3	59	80
15	12.5	14.6	61.2	38.8	88	108

^aDetermined by XPS. ^bFilms calcinated at 550 °C for 1 h. Determined from four probe resistivity measurements.

actual Sb molar ratio in ATO nanoparticles does mirror the content in the starting antimony and tin precursors and that the distribution of Sb dopant is homogeneous within the nanoparticles without significant surface enrichment in the ATO nanocrystals.

The coexistence of Sb⁵⁺ and Sb³⁺ in the nanoparticles with a ~20% excess of Sb⁵⁺ provides evidence for a conductivity arising from net free donor electrons. Substitution of Sb⁵⁺ for Sn⁴⁺ ions in the particles introduces a shallow donor level close to the conduction band of SnO₂, while the Sb³⁺ doping forms a

shallow acceptor level close to the valence band.³⁵ As-synthesized ATO nanocrystals were yellowish probably due to an Sb³⁺ → Sb⁵⁺ intervalence transfer absorption or absorptions.³⁶

Amphiphilic PVC-g-POEM graft copolymers **G1** and **G2** at different PVC to POEM ratios (**G1**, PVC:POEM = 4:6 wt %; **G2**, PVC:POEM = 7:3 wt %) were synthesized through atom transfer radical polymerization (ATRP) (SI). The microphase separation of hydrophilic POEM side chains (glass transition temperature, $T_g = -58$ °C) and hydrophobic PVC main chains ($T_g = 70$ °C)³⁷ drive PVC-g-POEM self-assembly to nanomicelles with the procedure carried out with added THF. THF is a good solvent for both PVC and POEM (solubility parameter, δ , $\delta_{\text{THF}} = 9.5$, $\delta_{\text{PVC}} = 9.6$, and $\delta_{\text{POEM}} = 10.8 \text{ cal}^{1/2} \text{ cm}^{-3/2}$) (Figure S4). Consequently, both PVC and POEM chains are highly stretched in THF. Introduction of HCl/H₂O selectively reduces the swelling of the PVC chains owing to the unfavorable interaction between PVC and the solvent, and micelles form with PVC cores and POEM coronas (Scheme 1). The micelle size, as measured from TEM images, was ~34 nm (**G1**) and ~40 nm (**G2**).

In order to make mesoporous films, freshly prepared ATO nanocrystals were added to THF solutions in which PVC-g-POEM had been predissolved. As-synthesized ATO nanocrystals had good hydrophilicities. According to TGA analysis, they contained 10–50 wt % organic, most likely adsorbed benzyl alcohol (Figure S1), which was advantageous for POEM side chain tethering to nanoparticle surfaces. Fourier transform infrared (FTIR) measurements illustrated a shifting of part of the ether (−O−) stretching band in POEM domains from 1098 to 1064 cm⁻¹ due to interaction with ATO nanoparticles with the remaining band nearly unchanged (Figure S6). The templating of PVC-g-POEM originates from the balance between adsorption enthalpy gain for the POEM/ATO interaction and conformational entropy loss of POEM domain stretching to incorporate nanocrystals.¹⁸

With unwashed ATO nanocrystals, worm-like structures with small mesopores (<6 nm) were formed. This is probably due to the disappearance of PVC-g-POEM micelles with excess benzyl alcohol (Figure S7).

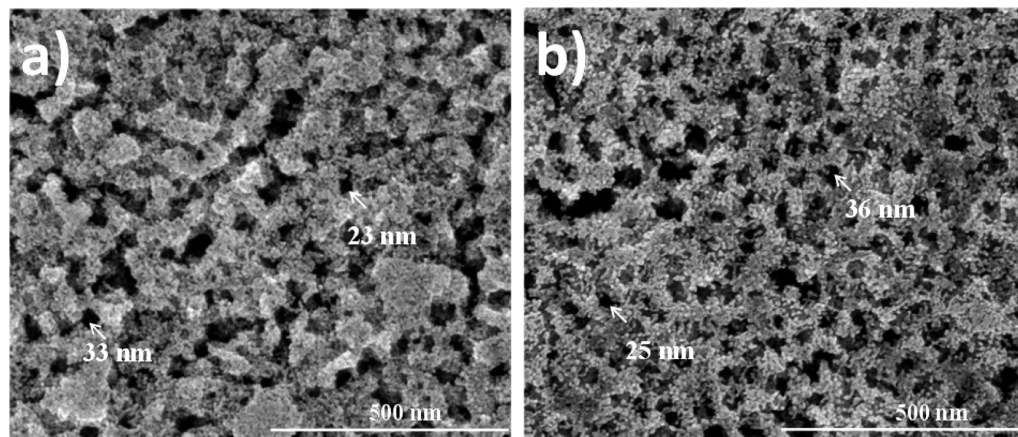


Figure 3. SEM images of mesoporous ATO nanocrystal films formed by using PVC-g-POEM as templates. (a) 10% ATO film templating by **G1** and (b) 8% ATO film templating by **G2**, respectively.

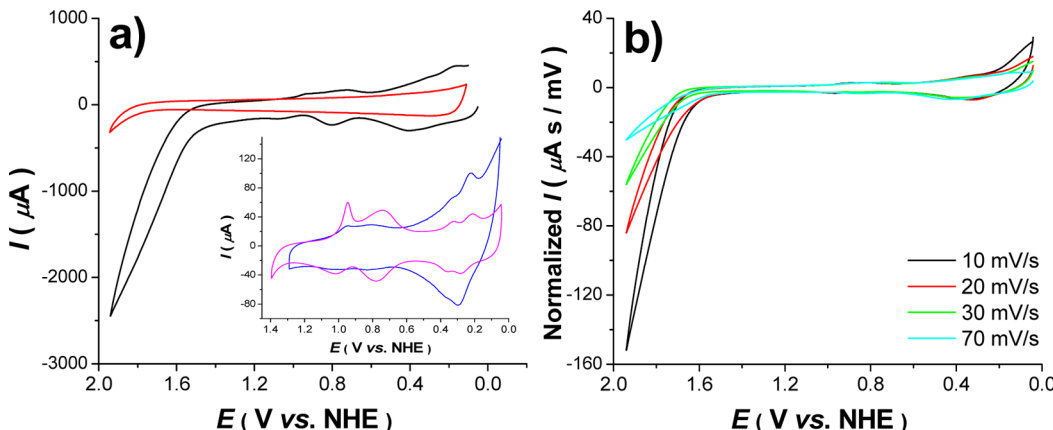


Figure 4. (a) Cyclic voltammograms in pH 5 acetate buffer ($\text{CH}_3\text{CO}_2\text{Na} = 0.073 \text{ M}$; $\text{CH}_3\text{CO}_2\text{H} = 0.027 \text{ M}$; $I = 0.5 \text{ M}$ with NaClO_4) of FTO|*nanoATO*-Ru^{II}-OH₂²⁺ electrodes previously loaded with 1-PO₃H₂ at 50 mV/s (dark line). The red line is the FTO|*nanoATO* background under the same experimental conditions. The inset shows CVs of FTO|*nanoATO*|1-PO₃H₂ at pH 5 after scanning to 1.5 V (violet line) and scanning to 1.9 V (blue line) at 10 mV/s. (b) Normalized ($i/\text{scan rate}$) cyclic voltammograms for FTO|*nanoATO*|1-PO₃H₂ in pH 5 acetate buffer at different scan rates. Sb% molar ratio = 10%.

Washed ATO nanoparticles were assembled into mesoporous films with PVC-g-POEM as templates with characteristically large, 20–40 nm mesopores (Figure 3, S8). ATO films templated by G1 and G2 resulted in similar mesopore sizes after removal of the polymer by nanoparticle sintering at 550 °C.

Comparisons between G1 and G2 templated films pointed to smaller wall thicknesses and improved ordering. This is probably due to the lower content of POEM side chains in G2 and to the higher fraction of POEM monomers tethered to the ATO nanoparticles. The latter implies that enthalpy gain is the dominant driving force in the interplay between the polymer and ATO.³⁸ In addition, the polymer/ATO assembly was influenced by the antimony doping ratio by varying the surface charge of the ATO nanocrystals.¹⁹ Mesoscopic aggregation increased as the amount of Sb dopant was decreased. This resulted in decreased transparency from 15% to 6% in ATO films. Highly transparent mesoporous ATO films were accessible when Sb was present in excess of 8%. This level of doping was accompanied by a transition in color from being yellowish to bluish after calcination owing to a red to NIR plasma free electron absorption.³⁹ The onset of UV-visible absorption at ~450 nm was consistent with literature observations (Figure S9a).⁴⁰ Both crystallinity and size of ATO nanocrystals increased to ~5 nm at 400 and 550 °C after calcination, as estimated from XRD patterns by the Scherrer formula (Figure S9b).⁹ Based on N₂ adsorption isotherms, Figure S9c, mesoporous ATO was calculated to have a high surface area of 120 $\text{m}^2 \text{ g}^{-1}$ with a total pore volume of 0.247 $\text{cm}^3 \text{ g}^{-1}$ and porosity of 62% (density: 6.73 g/cm^3).⁴¹

The resistivity for mesoporous ATO films of varying Sb-doping levels is summarized in Table 1 as obtained by four probe measurements. The films had resistivities ranging from 30 to 110 $\Omega \cdot \text{cm}$, which were positively correlated with Sb doping levels and in good agreement with the literature values.⁴² The smaller resistivity for G1 templated ATO films compared to G2 may originate from the thicker internal wall thickness of the latter.

Electrocatalytic Water Oxidation. Catalyst derivatized Sn(IV)-doped In₂O₃ (*nanoITO*) films have been shown to be successful substrates for water oxidation electrocatalysis. In this application, advantage is taken of fast electron transfer and

optical transparency that allows UV-visible spectral monitoring of the attached catalyst or catalysts.^{43,44} *nanoATO* films were investigated as alternates to *nanoITO* films in electrochemical catalysis by immobilizing the surface-bound catalyst [Ru^{II}(Mebimpy)(4,4'-(PO₃H₂)₂bpy)]²⁺(1-PO₃H₂: Mebimpy is 2,6-bis(1-methylbenzimidazol-2-yl)pyridine, Scheme 1). 1-PO₃H₂ is a new derivative of the well-known solution water oxidation catalyst, [Ru^{II}(Mebimpy)(2,2'-bpy)]²⁺(2-PO₃H₂, Figure S5).⁴⁵ After soaking *nanoATO* films in a 50 μM 1-PO₃H₂ methanol solution overnight, the resulting UV-visible spectrum was dominated by an intense Metal-to-Ligand Charge Transfer (MLCT) band at $\lambda_{\text{max}} = 498 \text{ nm}$ (Figure S10a).

The extent of surface loading of the catalyst (Γ in $\text{mol} \cdot \text{cm}^{-2}$) was first calculated from UV-visible measurements (Equation S1).⁴⁶ Typical saturated surface coverages of $2.48 \times 10^{-8} \text{ mol cm}^{-2}$ (2 μm) were obtained. Surface coverages were also obtained by the integration of current–potential waveforms for the Ru^{III}-OH²⁺/Ru^{II}-OH₂²⁺ wave in the absence of substrate by use of Equation S2.⁴⁷ Electrochemical evaluation gave $\Gamma_{\text{echem}} = 1.58 \times 10^{-8} \text{ mol cm}^{-2}$ (Figure S10b). Comparison of loadings from UV-visible and electrochemical measurements showed that 64% of the catalyst sites on FTO|*nanoATO*|1-PO₃H₂ were electroactive. This result demonstrates that FTO|*nanoATO* electrodes contain more electrochemically accessible catalyst sites than previously reported for RVC|*nanoITO* films.⁴⁸ Surface coverages on the high surface *nanoATO* electrodes are comparable to coverages obtained earlier for *nanoITO* electrodes of similar thicknesses and 2 orders of magnitude higher than loadings on planar FTO or ITO electrodes ($\sim 1.2 \times 10^{-10} \text{ mol cm}^{-2}$).^{43,45}

1-PO₃H₂ functionalized FTO|*nanoATO* electrodes exhibited the expected linear behavior in peak current with scan rate for the Ru^{III}-OH²⁺/Ru^{II}-OH₂²⁺ wave as a function of scan rate in the range from 5 to 50 mV/s in Figure S11. These results are consistent with kinetically facile electron transfer to and from the surface-bound complex, comparable to *nanoITO* electrodes.^{43,45} Peak-to-peak splittings ($\Delta E_p = E_{p,a} - E_{p,c}$) were less than 50 mV at low scan rate ($\leq 10 \text{ mV/s}$). At higher scan rates ($\geq 70 \text{ mV/s}$), ΔE_p increased, and peak currents deviated from a linear dependence on scan rate. Compared to 2-PO₃H₂ with $E_{1/2} \sim 0.68 \text{ V}$,⁴⁹ $E_{1/2}$ for the Ru^{III}-OH²⁺/Ru^{II}-OH₂²⁺ couple of

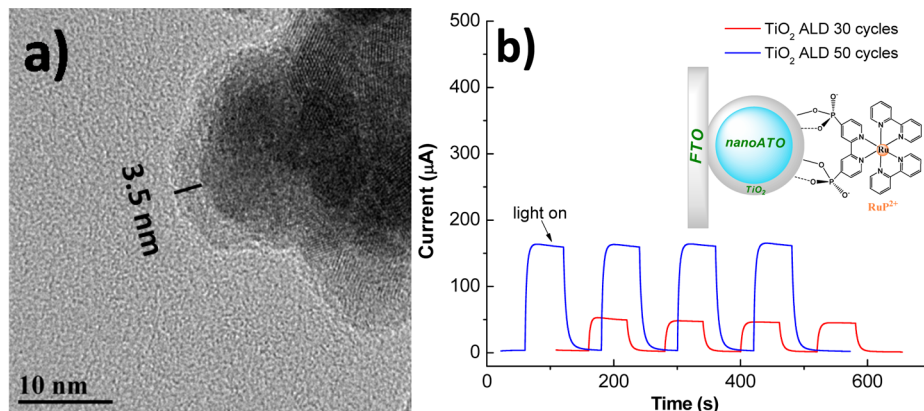


Figure 5. (a): HRTEM image of a G1 templated mesoporous 10% ATO atomic layer deposited with 50 cycles of a TiO₂ layer. TiO₂ shell thickness is 3.5 nm. (b): Photocurrents for a 10% nanoATO/TiO₂ core–shell photoanode derivatized with -RuP²⁺, FTO|nanoATO|TiO₂(3.5 nm)|-RuP²⁺, with an applied bias of 0.2 V vs NHE under 1.52 mW 445 nm irradiation in 20 mM aqueous EDTA⁴⁻ in 0.1 M LiClO₄.

1-PO₃H₂ was shifted positively to ~0.75 V due to the electron-withdrawing substituent effect of the -PO₃H₂ groups at the 4,4'-bpy positions. Sequential pH dependent waves appeared at 0.98 V for the Ru^{III}OH²⁺/Ru^{IV} = O²⁺ couple on the surface (**Figure 4a** inset). Similar to 2-PO₃H₂ in solution, this couple is kinetically inhibited by the kinetic requirement for proton loss from Ru^{III}OH²⁺ in its oxidation to Ru^{IV} = O²⁺. The narrow, skewed reduction wave at $E_{p,c} = 0.88$ V arises from Ru^{IV} = O²⁺ rereduction to Ru^{III}O⁺ followed by rapid protonation to give Ru^{III}OH²⁺.^{44,47}

As described earlier for 2-PO₃H₂ in solution, new pH-dependent waves appear following an oxidative scan past the water oxidation catalytic onset. They appear at $E_{1/2} = 0.25$ and 0.34 V at the expense of the Ru^{III}-OH²⁺/Ru^{II}-OH²⁺ couple and have been assigned to the surface couples of a pseudostable peroxide complex, Ru^{III}-OOH²⁺/Ru^{II}(HOOH)²⁺ and Ru^{IV}(OO)²⁺/Ru^{III}-OOH²⁺.^{44,50,51} A pH-independent Ru^V = O³⁺/Ru^{IV} = O²⁺ couple, slightly discernible at low pH, appeared after 1.6 V. It coincides with and triggers catalytic water oxidation with the catalytic current significantly larger than for a bare nanoATO film under the same condition.⁵⁰

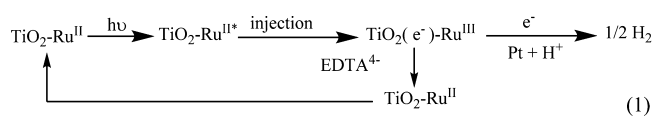
A Pourbaix ($E_{1/2}$ vs pH) diagram for 1-PO₃H₂ bound to nanoATO is shown in **Figure S12a**. For normalized scan rate CVs (i_p , i/v) in **Figure 4b**, catalytic currents increased with decreasing scan rate consistent with a rate limiting step prior to electron transfer at the electrode. Based on the electrochemical data for 1-PO₃H₂ in nanoATO, 1-PO₃H₂ appears to function similarly to 2-PO₃H₂ in solution. Water oxidation catalysis appears to occur by single site catalysis with rate limiting O atom transfer from Ru^V = O³⁺ to H₂O occurring in concert with proton transfer to an added base or the solvent by atom-proton transfer (APT), note in **Figure S12b**.^{52,53}

An approximate rate constant for water oxidation catalysis, k_{obs} , for 1-PO₃H₂ on nanoATO was evaluated by peak current ratio measurements following **Equation S3**.^{52,54} Based on CVs for 1-PO₃H₂ bound to nanoATO in pH 5 acetate buffer, [CH₃COO⁻] = 0.73 M, and in 0.1 M HClO₄ (**Figure S13**), k_{obs} was 0.29 s⁻¹ at pH 5 in acetate buffer and 0.03 s⁻¹ in 0.1 M HClO₄. The 10-fold increase in water oxidation rate at pH 5 with added CH₃COO⁻ is attributable to added acetate acting as the base and utilization of an APT pathway.

Photoelectrochemical H₂ Production. Core/shell photoanodes consisting of mesoporous conductive metal oxide cores of nanoITO with thin shells of wide-band gap TiO₂ have been

successfully applied in DSSC and DSPEC applications by taking advantage of the interfacial electron transfer characteristics of the TCO core material.^{26,55} In the present work, outer shells of TiO₂ were deposited on the mesoporous ATO films with the resulting core/shell structures investigated with nanoATO as a high surface area replacement for nanoITO. Mesoporous crystalline nanoATO films were coated with an amorphous TiO₂ shell to give core/shell nanoATO/TiO₂ films by atomic layer deposition (ALD) as described earlier for deposition on nanoITO.²⁵ High-resolution transmission electron microscopy (HRTEM) images demonstrated TiO₂ shell thicknesses of 1.9 and 3.5 nm resulting from 30 and 50 deposition cycles with the instrument used (**Figure 5a**).

Photoelectrochemical cells for H₂ production based on surface-bound [Ru(bpy)₂(4,4-(PO₃H₂)₂bpy)]²⁺ (-RuP²⁺; **Scheme 1**) derivatized TiO₂ or Nb₂O₅ on FTO with added ethylenediaminetetraacetic tetra-anion (EDTA⁴⁻) as the reductive scavengers in aqueous solutions have been described.^{56,57} Mesoporous nanoATO/TiO₂ core–shell photoanodes were investigated in the same configuration. Photocurrent measurements on -RuP²⁺ surface-derivatized nanoATO/TiO₂ photoanodes on FTO with a 0.2 V applied bias vs NHE under steady state 1.52 mW, 445 nm light irradiation in 20 mM EDTA⁴⁻ are shown in **Figure 5b**. They reveal that the photocurrent response is shell thickness dependent with a higher photocurrent for the nanoATO | TiO₂(3.5 nm) core/shell than for the 1.9 nm TiO₂ shell structure. EDTA⁴⁻ (20 mM) was added as a scavenger to reduce -RuP³⁺ following excitation and injection by -RuP²⁺, **eq 1**, resulting in sustained photocurrents and production of H₂ at the cathode.



Evolved hydrogen was measured by quantitative gas chromatography (GC) after 20 min of irradiation. The H₂ quantum efficiency (Φ_{H_2}) for a FTO|nanoATO|TiO₂(3.5 nm)|-RuP²⁺ sample was determined to be 18% with a 73% Faradaic efficiency (Φ_{Fa}) for captured H₂ (**Equations S4** and **S5**). The efficiency of H₂ production was comparable to results obtained on nanoTiO₂ under the same conditions with 15% Φ_{H_2} and 92% Φ_{Fa} .⁵⁷ Under the conditions of these experiments, rereduction of -Ru^{III} on the surface by EDTA⁴⁻ is

known to be rapid and quantitative.⁵⁷ The dimensions of the core/shell are important. For the *nanoATO*/ TiO_2 (1.9 nm) sample, H_2 and Faradaic efficiencies were substantially lower, 1% Φ_{H_2} and 30% Φ_{Fa} .

The results described here are important in demonstrating the use of the *nanoATO*/ TiO_2 core/shell in a DSPEC configuration for H_2 generation. The absence of a dependence on the oxide core, whether *nanoATO* or *nanoTiO₂* under these conditions, is consistent with interfacial dynamics controlled by reduction of photoproduced -RuP³⁺ by EDTA⁴⁻ at the interface.

CONCLUSIONS

We have successfully synthesized mesoporous ATO films by combining ATO nanocrystals and the graft copolymers PVC-g-POEM. ATO nanoparticles were conveniently synthesized by a benzyl alcohol assisted nonaqueous sol gel route under microwave irradiation, which allowed for control of antimony doping, size, and crystallinity. ATO electrodes with high surface areas and large mesopores were obtained by premade nanocrystal templating with the graft copolymers PVC-g-POEM. Mesoporous *nanoATO* films proved to be suitable alternatives to *nanoITO* in electrochemical catalysis with an added, surface-bound ruthenium water oxidation catalyst. A core/shell structure consisting of a mesoporous *nanoATO*/ nmTiO_2 film on FTO derivatized with RuP²⁺ was used to generate H_2 photoelectrochemically with ethylenediaminetetraacetic tetra-anion (EDTA⁴⁻) added as a reductive scavenger.

ASSOCIATED CONTENT

Supporting Information

The Supporting Information is available free of charge on the ACS Publications website at DOI: [10.1021/acsami.5b06348](https://doi.org/10.1021/acsami.5b06348).

Experimental details, characterization data, electrochemistry, catalysis, and equations ([PDF](#))

AUTHOR INFORMATION

Corresponding Author

*E-mail: tjmeyer@unc.edu.

Notes

The authors declare no competing financial interest.

ACKNOWLEDGMENTS

This research was supported solely by the UNC EFRC: Center for Solar Fuels, an Energy Frontier Research Center funded by the U.S. Department of Energy, Office of Science, Office of Basic Energy Sciences under Award Number DE-SC0001011. We acknowledge a Royster Society Fellowship at UNC for support of H.L. We thank the Chapel Hill Analytical and Nanofabrication Laboratory for XPS measurements and imaging. We also thank Prof. Wenbin Lin for BET measurements and Prof. Valerie Ashby for TGA and GPC analysis.

REFERENCES

- (1) Armstrong, N. R.; Veneman, P. A.; Ratcliff, E.; Placencia, D.; Brumbach, M. Oxide Contacts in Organic Photovoltaics: Characterization and Control of Near-Surface Composition in Indium–Tin Oxide (ITO) Electrodes. *Acc. Chem. Res.* **2009**, *42*, 1748–1757.
- (2) Walzer, K.; Maennig, B.; Pfeiffer, M.; Leo, K. Highly Efficient Organic Devices Based on Electrically Doped Transport Layers. *Chem. Rev.* **2007**, *107*, 1233–1271.
- (3) Forman, A. J.; Chen, Z.; Chakthranont, P.; Jaramillo, T. F. High Surface Area Transparent Conducting Oxide Electrodes with a Customizable Device Architecture. *Chem. Mater.* **2014**, *26*, 958–964.
- (4) Yang, Z.; Gao, S.; Li, T.; Liu, F.-Q.; Ren, Y.; Xu, T. Enhanced Electron Extraction from Template-Free 3D Nanoparticulate Transparent Conducting Oxide (TCO) Electrodes for Dye-Sensitized Solar Cells. *ACS Appl. Mater. Interfaces* **2012**, *4*, 4419–4427.
- (5) Müller, V.; Rathousky, J.; Fattakhova-Rohlfing, D. Covalent Immobilization of Redox Protein within the Mesopores of Transparent Conducting Electrodes. *Electrochim. Acta* **2014**, *116*, 1–8.
- (6) Aksu, Y.; Frasca, S.; Wollenberger, U.; Driess, M.; Thomas, A. A Molecular Precursor Approach to Tunable Porous Tin-Rich Indium Tin Oxide with Durable High Electrical Conductivity for Bioelectronic Devices. *Chem. Mater.* **2011**, *23*, 1798–1804.
- (7) Kent, C. A.; Concepcion, J. J.; Dares, C. J.; Torelli, D. A.; Rieth, A. J.; Miller, A. S.; Hoertz, P. G.; Meyer, T. J. Water Oxidation and Oxygen Monitoring by Cobalt-Modified Fluorine-Doped Tin Oxide Electrodes. *J. Am. Chem. Soc.* **2013**, *135*, 8432–8435.
- (8) Fattakhova-Rohlfing, D.; Brezesinski, T.; Rathouský, J.; Feldhoff, A.; Oekermann, T.; Wark, M.; Smarsly, B. M. Transparent Conducting Films of Indium Tin Oxide with 3D Mesopore Architecture. *Adv. Mater.* **2006**, *18*, 2980–2983.
- (9) Hou, K.; Puzzo, D.; Helander, M. G.; Lo, S. S.; Bonifacio, L. D.; Wang, W.; Lu, Z.-H.; Scholes, G. D.; Ozin, G. A. Dye-Anchored Mesoporous Antimony-Doped Tin Oxide Electrochemiluminescence Cell. *Adv. Mater.* **2009**, *21*, 2492–2496.
- (10) Gordon, R. G. Criteria for Choosing Transparent Conductors. *MRS Bull.* **2000**, *25*, 52–57.
- (11) Chopra, K. L.; Major, S.; Pandya, D. K. Transparent Conductors—A Status Review. *Thin Solid Films* **1983**, *102*, 1–46.
- (12) Deng, Y.; Wei, J.; Sun, Z.; Zhao, D. Large-pore Ordered Mesoporous Materials Templated from Non-Pluronic Amphiphilic Block Copolymers. *Chem. Soc. Rev.* **2013**, *42*, 4054–4070.
- (13) Kresge, C. T.; Leonowicz, M. E.; Roth, W. J.; Vartuli, J. C.; Beck, J. S. Ordered Mesoporous Molecular Sieves Synthesized by a Liquid-crystal Template Mechanism. *Nature* **1992**, *359*, 710–712.
- (14) Wan, Y.; Zhao. On the Controllable Soft-Templating Approach to Mesoporous Silicates. *Chem. Rev.* **2007**, *107*, 2821–2860.
- (15) Pan, J. H.; Zhao, X. S.; Lee, W. I. Block Copolymer-templated Synthesis of Highly Organized Mesoporous TiO_2 -based Films and their Photoelectrochemical Applications. *Chem. Eng. J.* **2011**, *170*, 363–380.
- (16) Bucknall, D. G.; Anderson, H. L. Polymers Get Organized. *Science* **2003**, *302*, 1904–1905.
- (17) Wang, Y.; Brezesinski, T.; Antonietti, M.; Smarsly, B. Ordered Mesoporous Sb-, Nb-, and Ta-Doped SnO_2 Thin Films with Adjustable Doping Levels and High Electrical Conductivity. *ACS Nano* **2009**, *3*, 1373–1378.
- (18) Buonsanti, R.; Pick, T. E.; Krins, N.; Richardson, T. J.; Helms, B. A.; Milliron, D. J. Assembly of Ligand-Stripped Nanocrystals into Precisely Controlled Mesoporous Architectures. *Nano Lett.* **2012**, *12*, 3872–3877.
- (19) Müller, V.; Rasp, M.; Rathouský, J.; Schütz, B.; Niederberger, M.; Fattakhova-Rohlfing, D. Transparent Conducting Films of Antimony-Doped Tin Oxide with Uniform Mesostructure Assembled from Preformed Nanocrystals. *Small* **2010**, *6*, 633–637.
- (20) Müller, V.; Rasp, M.; Štefanić, G.; Ba, J.; Günther, S.; Rathouský, J.; Niederberger, M.; Fattakhova-Rohlfing, D. Highly Conducting Nanosized Monodispersed Antimony-Doped Tin Oxide Particles Synthesized via Nonaqueous Sol–Gel Procedure. *Chem. Mater.* **2009**, *21*, 5229–5236.
- (21) Yu, C.; Fan, J.; Tian, B.; Stucky, G. D.; Zhao, D. Synthesis of Mesoporous Silica from Commercial Poly(ethylene oxide)/Poly(butylene oxide) Copolymers: Toward the Rational Design of Ordered Mesoporous Materials. *J. Phys. Chem. B* **2003**, *107*, 13368–13375.
- (22) Ahn, S. H.; Chi, W. S.; Kim, D. J.; Heo, S. Y.; Kim, J. H. Honeycomb-Like Organized TiO_2 Photoanodes with Dual Pores for

- Solid-State Dye-Sensitized Solar Cells. *Adv. Funct. Mater.* **2013**, *23*, 3901–3908.
- (23) Ahn, S. H.; Chi, W. S.; Park, J. T.; Koh, J. K.; Roh, D. K.; Kim, J. H. Direct Assembly of Preformed Nanoparticles and Graft Copolymer for the Fabrication of Micrometer-thick, Organized TiO₂ Films: High Efficiency Solid-state Dye-sensitized Solar Cells. *Adv. Mater.* **2012**, *24*, 519–522.
- (24) Ba, J.; Polleux, J.; Antonietti, M.; Niederberger, M. Non-aqueous Synthesis of Tin Oxide Nanocrystals and Their Assembly into Ordered Porous Mesostructures. *Adv. Mater.* **2005**, *17*, 2509–2512.
- (25) Alibabaei, L.; Brennaman, M. K.; Norris, M. R.; Kalanyan, B.; Song, W.; Losego, M. D.; Concepcion, J. J.; Binstead, R. A.; Parsons, G. N.; Meyer, T. J. Solar Water Splitting in a Molecular Photoelectrochemical Cell. *Proc. Natl. Acad. Sci. U. S. A.* **2013**, *110*, 20008–20013.
- (26) Correa Baena, J. P.; Agrios, A. G. Antimony-Doped Tin Oxide Aerogels as Porous Electron Collectors for Dye-Sensitized Solar Cells. *J. Phys. Chem. C* **2014**, *118*, 17028–17035.
- (27) Alibabaei, L.; Farnum, B. H.; Kalanyan, B.; Brennaman, M. K.; Losego, M. D.; Parsons, G. N.; Meyer, T. J. Atomic Layer Deposition of TiO₂ on Mesoporous nanoITO: Conductive Core–Shell Photoanodes for Dye-Sensitized Solar Cells. *Nano Lett.* **2014**, *14*, 3255–3261.
- (28) Cushing, B. L.; Kolesnichenko, V. L.; O'Connor, C. J. Recent Advances in the Liquid-Phase Syntheses of Inorganic Nanoparticles. *Chem. Rev.* **2004**, *104*, 3893–3946.
- (29) Niederberger, M. Nonaqueous Sol–Gel Routes to Metal Oxide Nanoparticles. *Acc. Chem. Res.* **2007**, *40*, 793–800.
- (30) Bilecka, I.; Djerdj, I.; Niederberger, M. One-minute Synthesis of Crystalline Binary and Ternary Metal Oxide Nanoparticles. *Chem. Commun.* **2008**, 886–888.
- (31) Pinna, N.; Neri, G.; Antonietti, M.; Niederberger, M. Nonaqueous Synthesis of Nanocrystalline Semiconducting Metal Oxides for Gas Sensing. *Angew. Chem., Int. Ed.* **2004**, *43*, 4345–4349.
- (32) Hu, M.; Xu, J.; Gao, J.; Yang, S.; Wong, J. S. P.; Li, R. K. Y. Benzyl Alcohol-based Synthesis of Oxide Nanoparticles: the Perspective of SNI Reaction Mechanism. *Dalton Trans.* **2013**, *42*, 9777–9784.
- (33) Luo, L.; Bozyigit, D.; Wood, V.; Niederberger, M. High-Quality Transparent Electrodes Spin-Cast from Preformed Antimony-Doped Tin Oxide Nanocrystals for Thin Film Optoelectronics. *Chem. Mater.* **2013**, *25*, 4901–4907.
- (34) da Silva, R. O.; Conti, T. G.; de Moura, A. F.; Stroppa, D. G.; Freitas, L. C. G.; Ribeiro, C.; Camargo, E. R.; Longo, E.; Leite, E. R. Antimony-Doped Tin Oxide Nanocrystals: Synthesis and Solubility Behavior in Organic Solvents. *ChemPhysChem* **2009**, *10*, 841–846.
- (35) Thangaraju, B. Structural and Electrical Studies on Highly Conducting Spray Deposited Fluorine and Antimony Doped SnO₂ Thin Films from SnCl₂ Precursor. *Thin Solid Films* **2002**, *402*, 71–78.
- (36) Rockenberger, J.; zum Felde, U.; Tischer, M.; Tröger, L.; Haase, M.; Weller, H. Near Edge X-ray Absorption Fine Structure Measurements (XANES) and Extended x-ray Absorption Fine Structure Measurements (EXAFS) of the Valence State and Coordination of Antimony in Doped Nanocrystalline SnO₂. *J. Chem. Phys.* **2000**, *112*, 4296–4304.
- (37) Roh, D. K.; Park, J. T.; Ahn, S. H.; Ahn, H.; Ryu, D. Y.; Kim, J. H. Amphiphilic Poly(vinyl chloride)-g-poly(oxyethylene methacrylate) Graft Polymer Electrolytes: Interactions, Nanostructures and Applications to Dye-sensitized solar cells. *Electrochim. Acta* **2010**, *55*, 4976–4981.
- (38) Milliron, D. J.; Buonsanti, R.; Llordes, A.; Helms, B. A. Constructing Functional Mesostructured Materials from Colloidal Nanocrystal Building Blocks. *Acc. Chem. Res.* **2014**, *47*, 236–246.
- (39) Nütz, T.; Felde, U. z.; Haase, M. Wet-chemical Synthesis of Doped Nanoparticles: Blue-colored Colloids of n-doped SnO₂:Sb. *J. Chem. Phys.* **1999**, *110*, 12142–12150.
- (40) Sharma, S.; Volosin, A. M.; Schmitt, D.; Seo, D.-K. Preparation and Electrochemical Properties of Nanoporous Transparent Antimony-doped Tin Oxide (ATO) Coatings. *J. Mater. Chem. A* **2013**, *1*, 699–706.
- (41) Wu, J.; Chen, F.; Shen, Q.; Schoenung, J. M.; Zhang, L. Spark Plasma Sintering and Densification Mechanisms of Antimony-doped Tin Oxide Nanoceramics. *J. Nanomater.* **2013**, *2013*, 561895.
- (42) Peng, Q.; Kalanyan, B.; Hoertz, P. G.; Miller, A.; Kim, D. H.; Hanson, K.; Alibabaei, L.; Liu, J.; Meyer, T. J.; Parsons, G. N.; Glass, J. T. Solution-Processed, Antimony-Doped Tin Oxide Colloid Films Enable High-Performance TiO₂ Photoanodes for Water Splitting. *Nano Lett.* **2013**, *13*, 1481–1488.
- (43) Hoertz, P. G.; Chen, Z.; Kent, C. A.; Meyer, T. J. Application of High Surface Area Tin-Doped Indium Oxide Nanoparticle Films as Transparent Conducting Electrodes. *Inorg. Chem.* **2010**, *49*, 8179–8181.
- (44) Chen, Z.; Vannucci, A. K.; Concepcion, J. J.; Jurss, J. W.; Meyer, T. J. Proton-coupled Electron Transfer at Modified Electrodes by Multiple Pathways. *Proc. Natl. Acad. Sci. U. S. A.* **2011**, *108*, E1461–E1469.
- (45) Chen, Z.; Concepcion, J. J.; Jurss, J. W.; Meyer, T. J. Single-Site, Catalytic Water Oxidation on Oxide Surfaces. *J. Am. Chem. Soc.* **2009**, *131*, 15580–15581.
- (46) Trammell, S. A.; Meyer, T. J. Diffusional Mediation of Surface Electron Transfer on TiO₂. *J. Phys. Chem. B* **1999**, *103*, 104–107.
- (47) Vannucci, A. K.; Hull, J. F.; Chen, Z.; Binstead, R. A.; Concepcion, J. J.; Meyer, T. J. Water Oxidation Intermediates Applied to Catalysis: Benzyl Alcohol Oxidation. *J. Am. Chem. Soc.* **2012**, *134*, 3972–3975.
- (48) Méndez, M. A.; Alibabaei, L.; Concepcion, J. J.; Meyer, T. J. Electrocatalysis on Oxide-Stabilized, High-Surface Area Carbon Electrodes. *ACS Catal.* **2013**, *3*, 1850–1854.
- (49) Chen, Z.; Concepcion, J. J.; Hull, J. F.; Hoertz, P. G.; Meyer, T. J. Catalytic Water Oxidation on Derivatized nanoITO. *Dalton Trans.* **2010**, *39*, 6950–6952.
- (50) Concepcion, J. J.; Tsai, M.-K.; Muckerman, J. T.; Meyer, T. J. Mechanism of Water Oxidation by Single-Site Ruthenium Complex Catalysts. *J. Am. Chem. Soc.* **2010**, *132*, 1545–1557.
- (51) Concepcion, J. J.; Jurss, J. W.; Templeton, J. L.; Meyer, T. J. One Site is Enough. Catalytic Water Oxidation by [Ru(tpy)(bpm)(OH₂)]²⁺ and [Ru(tpy)(bpz)(OH₂)]²⁺. *J. Am. Chem. Soc.* **2008**, *130*, 16462–16463.
- (52) Vannucci, A. K.; Alibabaei, L.; Losego, M. D.; Concepcion, J. J.; Kalanyan, B.; Parsons, G. N.; Meyer, T. J. Crossing the Divide between Homogeneous and Heterogeneous Catalysis in Water Oxidation. *Proc. Natl. Acad. Sci. U. S. A.* **2013**, *110*, 20918–20922.
- (53) Chen, Z.; Concepcion, J. J.; Hu, X.; Yang, W.; Hoertz, P. G.; Meyer, T. J. Concerted O Atom–proton Transfer in the O–O Bond Forming Step in Water Oxidation. *Proc. Natl. Acad. Sci. U. S. A.* **2010**, *107*, 7225–7229.
- (54) Nakagawa, T.; Beasley, C. A.; Murray, R. W. Efficient Electro-Oxidation of Water near Its Reversible Potential by a Mesoporous IrO_x Nanoparticle Film. *J. Phys. Chem. C* **2009**, *113*, 12958–12961.
- (55) Song, W.; Vannucci, A. K.; Farnum, B. H.; Lapides, A. M.; Brennaman, M. K.; Kalanyan, B.; Alibabaei, L.; Concepcion, J. J.; Losego, M. D.; Parsons, G. N.; Meyer, T. J. Visible Light Driven Benzyl Alcohol Dehydrogenation in a Dye-Sensitized Photoelectrosynthesis Cell. *J. Am. Chem. Soc.* **2014**, *136*, 9773–9779.
- (56) Luo, H.; Song, W.; Hoertz, P. G.; Hanson, K.; Ghosh, R.; Rangan, S.; Brennaman, M. K.; Concepcion, J. J.; Binstead, R. A.; Bartynski, R. A.; Lopez, R.; Meyer, T. J. A Sensitized Nb₂O₅ Photoanode for Hydrogen Production in a Dye-Sensitized Photoelectrosynthesis Cell. *Chem. Mater.* **2013**, *25*, 122–131.
- (57) Song, W.; Brennaman, M. K.; Concepcion, J. J.; Jurss, J. W.; Hoertz, P. G.; Luo, H.; Chen, C.; Hanson, K.; Meyer, T. J. Interfacial Electron Transfer Dynamics for [Ru(bpy)₂((4,4'-PO₃H₂)₂bpy)]²⁺ Sensitized TiO₂ in a Dye-Sensitized Photoelectrosynthesis Cell: Factors Influencing Efficiency and Dynamics. *J. Phys. Chem. C* **2011**, *115*, 7081–7091.